(Preprint) AAS 693

ON THE RESONANT DYNAMICS OF PARTICLES IN NON-SYMMETRIC POTENTIALS

Lucia Francesca Civati[*], **Iosto Fodde**[*], **and Fabio Ferrari**[*]

The motion of particles around irregular asteroids is shaped by a complex gravitational environment that can lead to chaotic behavior. Nevertheless, stable dynamical structures such as resonances may emerge, possibly influencing the long-term evolution of orbiting debris, ejecta, or dust. This work focuses on the role of the asteroid's non-symmetric gravitational potential, with an application to the Didymos primary. By combining resonance theory, Hamiltonian approaches, Poincaré surface of section analysis, and chaos indicators, this study explores how dissipative forces representing inter-particle collisions can facilitate capture into resonant states, to explore the conditions under which transient or long-term trapping can occur.

INTRODUCTION

The dynamics around an irregularly shaped asteroid is inherently complex and often exhibits chaotic behavior, making the evolution of particle or spacecraft motion unpredictable. Despite this, it is possible to identify stable regions in the vicinity of such bodies, where periodic orbits and resonant motion can occur.

This work aims to characterize the dynamical structures arising from the asteroid's non-spherical gravity field, with particular attention to the formation of resonant pathways that, when combined with perturbative effects, influence whether particles become trapped or escape. We explore the mechanisms behind transient and long-term particle confinement, a phenomenon relevant to various processes such as moonlet formation, the evolution of debris clouds, the redistribution of surface material, and the emergence of ring-like features. A key example highlighting the dynamical relevance of such resonances is provided by the rings of Chariklo and Haumea, which are found to orbit near the second-order 1:3 resonance.[1]

While previous studies[2345] have explored similar problems using simplified models - such as ellipsoids, localized mass anomalies, or low-degree spherical harmonic expansions - this work adopts a high-fidelity gravity model that includes gravitational harmonics up to degree and order six, with an application to the primary of Didymos system, the binary asteroid target of the Hera mission, whose binary nature makes it a suitable case study for capture dynamics and secondary body formation. This more realistic representation reveals a rich variety of resonances that emerge due to the asteroid's complex shape.

Another relevant aspect of this study is the focus on resonances in the body-fixed frame, which provides a more natural and autonomous framework for analyzing motion near irregular bodies, linking them with classical ground-track resonance definitions.

[*]Department of Aerospace Science and Technology (DAER), Politecnico di Milano, Via La Masa 34, Milan, Italy

Then, to understand resonance and object trapping, this work examines capture mechanisms driven by perturbations relevant to particles and ejecta, which are the dissipative effects due to particle collisions, expanding the scope beyond the more commonly studied context of spacecraft maneuvering via low-thrust propulsion. Through the combined use of resonance analysis, Poincaré maps, Hamiltonian models, and dynamical indicators, the dynamical environment is analyzed and the conditions under which these perturbations may lead to transient capture are explored.

DYNAMICAL MODELING

The equations of motion for a generic particle orbiting a body in a body-fixed rotating frame are expressed by

$$\ddot{\mathbf{r}} = -2\dot{\theta} \times \dot{\mathbf{r}} - \dot{\theta} \times (\dot{\theta} \times \mathbf{r}) + \nabla U \tag{1}$$

To account for the irregular shape of a celestial body, such as an asteroid, its potential can be described through a spherical harmonics expansion, allowing to capture the deviation from sphericity due to mass distribution asymmetries, i.e.,

$$U = \frac{GM}{r} \sum_{n=0}^{\infty} \sum_{m=0}^{m} \frac{R_b^n}{r^n} P_{nm} sin(\phi)(\bar{C}_{nm} cos(m\lambda) + \bar{S}_{nm} sin(m\lambda)) \tag{2}$$

When studying resonances, it is useful to formulate the spherical harmonics expanded potential in terms of orbital elements (a, e, i, Ω, ω, M), as in Kaula's development.[6] In particular, the perturbing part of the potential can be expressed as

$$R = -\frac{GM}{a} \sum_{n=2}^{\infty} \sum_{m=0}^{m} \frac{R_b^n}{a^n} \sum_{p=0}^{n} F_{nmp}(i) \sum_{q=-\infty}^{\infty} G_{npq}(e) S_{nmpq}(M, \omega, \Omega, \theta) \tag{3}$$

The terms $F_{nmp}(i)$, $G_{npq}(e)$ are function of the inclination i, eccentricity e, respectively, while S_{nmpq} depends on the angular variables: periapsis argument ω, mean anomaly M, right ascension of the ascending node Ω, and sidereal time θ. The complete expression of these functions can be found in 7.

The term S_{nmpq}, which includes the spherical harmonics coefficients, enables the identification of specific resonances in the phase-space through an appropriate selection of the indices n, m, p, and q, as will be seen later.

$$S_{nmpq} = \begin{cases} C_{nm} \cos(\Psi_{nmpq}) + S_{nm} \sin(\Psi_{nmpq}) & \text{if } n\text{-}m \text{ is even,} \\ -S_{nm} \cos(\Psi_{nmpq}) + C_{nm} \sin(\Psi_{nmpq}) & \text{if } n\text{-}m \text{ is odd} \end{cases} \tag{4}$$

Here,

$$\Psi_{nmpq} = (n - 2p)\omega + (n - 2p + q)M + m(\Omega - \theta) \tag{5}$$

is the Kaula's phase angle. Finally, the Hamiltonian can be written as

$$H = -\frac{(GM)^2}{2L^2} + R_{ast} + \dot{\theta}\Lambda \tag{6}$$

where the quantity $L = \sqrt{GMa}$ is the momentum conjugated to $\lambda = \omega + \Omega + M$, with a semi-major axis, while Λ is the conjugated momentum to the sidereal time and the term $\Lambda\dot{\theta}$ accounts for the asteroid's rotation.

This formulation allows to adopt the Hamiltonian formalism as an analytical tool for investigating the structure of the phase-space and the resonance patterns induced by the irregular gravity field.

CHARACTERIZATION OF RESONANT MOTION

A resonance occurs when the rate of the Kaula's angle is zero

$$\dot{\Psi}_{nmpq} = (n-2p)\dot{\omega} + (n-2p+q)\dot{M} + m(\dot{\Omega} - \dot{\theta}) \simeq 0 \tag{7}$$

Considering the frequencies $\dot{\Omega}$ and $\dot{\omega}$ negligible, Eq. 7 reduces to the classical definition of ground-track resonance, that is the $p_1 : p_2$ commensurability relation between the rotational period of the central body and the rotational period of the massless particle, with $p_1, p_2 \in \mathbb{Z} - \{0\}$

$$p_1\dot{\theta} = p_2\dot{M} \tag{8}$$

where $\dot{M}$ denotes the mean motion of the object, associated with its orbital period in the inertial frame, and $\dot{\theta}$ is the rotational rate of the central body. Actually $\dot{\Omega}$ and $\dot{\omega}$ are small but not zero, so for different n, m, p and q the resonant angle derivative is zero at different locations, providing a multiplet of resonances.[3]

Combining Eq. 7 with Eq. 8 it is easy to identify the terms of n, m, p, and q and the associated combination of spherical harmonics coefficients that give rise to a specific resonance $p_1 : p_2$, enabling the identification and study of specific resonances within the system.

In the description of the Hamiltoinan phase space it is useful to introduce the so-called resonant angle $\sigma = p_2\lambda - p_1\theta$. To introduce σ and to keep the new variables canonical, a symplectic transformation is used, leading to the new set of canonical variables:

$$\begin{cases} \sigma = \sigma \\ L = p_2 L' \\ \Lambda = \Lambda' - p_1 L' \\ \theta' = \theta \end{cases} \tag{9}$$

Orbital elements are defined relatively to an inertial frame description; however, the investigation of stable and chaotic dynamics around an irregularly shaped small body is more naturally formulated in a body-fixed frame co-rotating with the central object. Indeed, in this frame the problem becomes autonomous, as the gravitational potential is stationary, allowing for the identification of resonance islands and stable regions through tools as Poincaré surfaces of section. However, the provided definition of commensurability condition is based on the inertial-frame dynamics, and does not directly translate to the body-fixed frame.

To provide a more intuitive and geometrically interpretable definition in the rotating frame, an alternative formulation can be adopted. Two fundamental frequencies can be introduced:[7] the radial (epicyclic) frequency $\kappa = \dot{M} - \dot{\omega}$, which corresponds to the rate at which the particle returns to the periapsis, and the synodic frequency $\dot{M} - \dot{\theta}$, which measures how often the particle returns to a fixed position in the rotating frame. Thus, the resonance condition becomes

$$j\kappa = k(\dot{M} - \dot{\theta}) \tag{10}$$

which corresponds to a $k : (k-j)$ resonance:

$$\frac{\dot{M}}{\dot{\theta}} \sim \frac{k}{k-j} \tag{11}$$

This definition has a direct geometric interpretation in the body-fixed frame. Specifically, j represents the number of braids, which means number of distinct types of sectors generated by the resonant periodic orbit, each corresponding to a qualitatively different portion of the resonant periodic orbit, while $|k|$ indicates the number of identical sectors. Equivalently, $|j|$ also represents the number of returns on the surface of section in the corresponding Poincarè map. The number of self-intersections in the trajectory is given by $|k|(j-1)$.

Illustrative examples of the p_1 = 2, p_2 = 5 resonance, which corresponds to a k = -2, j = 3 resonance in the body-fixed frame, and p_1 = 1, p_2 = 3 resonance (k = -1, j = 2), are shown in Fig. 1.
.

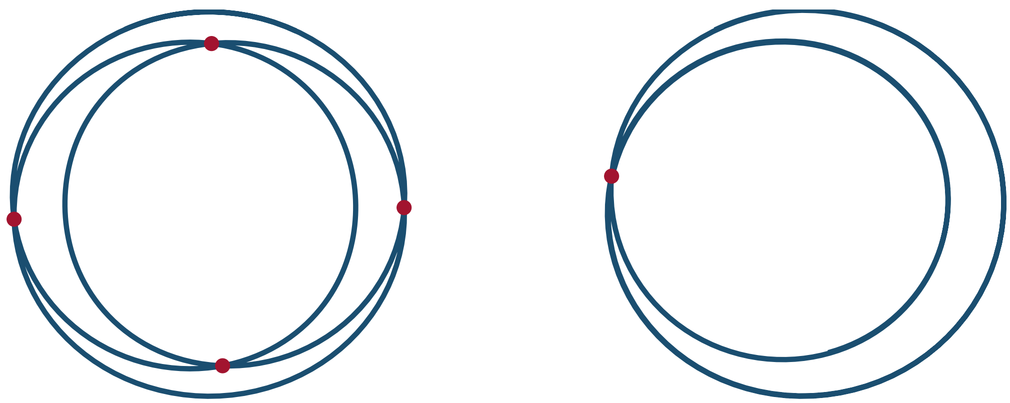

(a) 2:5 resonance.

(b) 1:3 resonance.

Figure 1: Examples of 2:5 (corresponding to $k = -2$, $j = 3$) and 1:3 ($k = -1$, $j = 2$) resonant periodic orbits in the body-fixed frame. Self-crossing points are marked in red. Braids and angular sectors can be distinguished in the corresponding resonant structures.

STABILITY MAPS AND CHAOTIC ZONES

To identify the main resonant structures around the body, phase space portraits are employed. These are computed on a 200×200 grid in the (M, a) and (a, e) plane by evaluating the Finite Time Lyapunov Exponent (FTLE) at each point, offering a clear picture of the local dynamical behavior.

FTLE maps are a practical tool for distinguishing regions with different stability properties and, in this context, help to identify and separate resonant zones in phase space. The FTLE indicator is chosen due to its straightforward computation and effectiveness in capturing local divergence of nearby trajectories, making it well-suited for resonance studies. More in detail, it quantifies the maximum rate of separation between infinitesimally close trajectories over a finite time interval and is defined as:[8]

$$\mathrm{FTLE}(\mathbf{x}_0)_{t_0}^{t_0+T} = \frac{1}{T} \ln \sqrt{\lambda_n(\mathbf{x}_0, t_0, T)} \tag{12}$$

where λ_n is the largest eigenvalue of the right Cauchy–Green deformation tensor Δ, which is given by:

$$\Delta = \left(\frac{d\Phi {t_0}^{t_0+T}(\mathbf{x})}{d\mathbf{x}}\right)^* \left(\frac{d\Phi {t_0}^{t_0+T}(\mathbf{x})}{d\mathbf{x}}\right) \tag{13}$$

Here, $\Phi_{t_0}^{t_0+T}$ denotes the flow map from initial time t_0 to $t_0 + T$, and the deformation tensor is computed from the state transition matrix (STM). Maximum stretching occurs along the direction corresponding to the largest eigenvalue of Δ.

A stability diagram is constructed by computing the Finite-Time Lyapunov Exponent (FTLE) over a grid of initial conditions in the (e, a) space, as shown in Fig. 2. For this analysis, the angular elements are fixed to $\nu = 0$, $\omega = 0$, $\Omega = 0$, and the inclination is set to $i = 0$. Similar stability maps have been extensively used in the literature to investigate chaotic regions around elongated bodies and contact binaries,[9] particularly in the context of Kepler maps, to identify resonances and delineate the boundaries of dynamical chaos. As in those studies, Fig. 2 reveals a ragged boundary separating the red chaotic region (characterized by high FTLE values) from the regular green domain. The "teeth"-like blue features along this border correspond to resonances. The width of these structures serves as a useful proxy for the resonance width in the (a, e) plane. By fixing the eccentricity, one can easily identify the locations and extent of resonant zones where the motion becomes chaotic. Initial conditions leading to collisions with the central body - typically corresponding to particles with pericenter distances smaller than the mean radius - are excluded from the map.

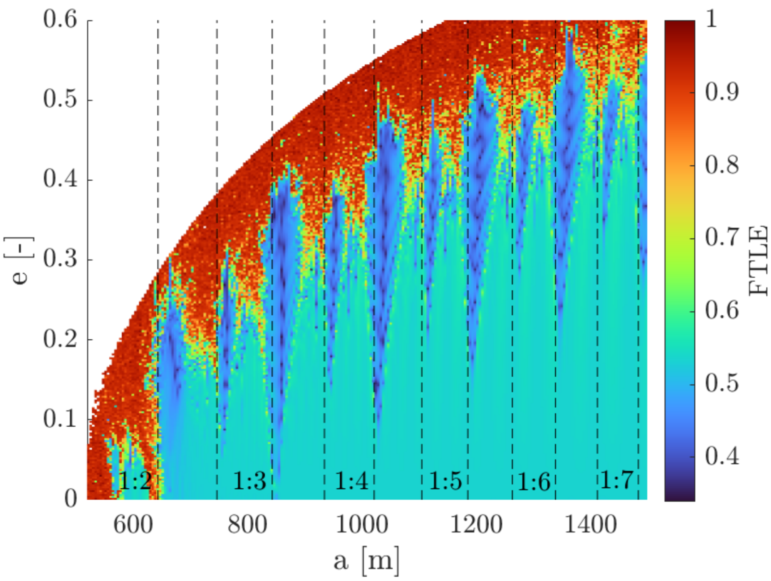

Figure 2: Stability diagram in the (a, e) plane. For each point in the grid the color represents the value of the FTLE for that initial condition normalized over the highest FTLE. The black vertical dashed lines represent the semi-major axis corresponding to a p_1:p_2 resonance, at the left of the relative line.

Generally, the chaotic region starts at smaller semi-major axes at low eccentricities and low-semi-major axis resonances are present just at low values of eccentricity. At higher eccentricities the width of the resonances is wider. Below the 1:2 resonance, the phase space tends to be predominantly chaotic across all tested eccentricities. The 1:3, 1:4, and 1:5 resonances appear as the most prominent, and their width increases with eccentricity.

To complement this analysis, FTLE phase portraits in the (M, a) plane are provided for various eccentricity values (with $i = 0°$) in Fig. 3, offering a broader view of the primary resonances around the central body. These plots illustrate how resonances emerge, evolve, and vary in amplitude with increasing eccentricity. The structures observed - both chaotic and regular - are consistent with those in the (e, a) stability map of Fig. 2, and further highlight the presence of resonance islands. In some cases, between the biggest islands, some features corresponding to other orders resonances appear. All the maps are generated using a Cartesian formulation and include all spherical harmonics up to degree and order 6.

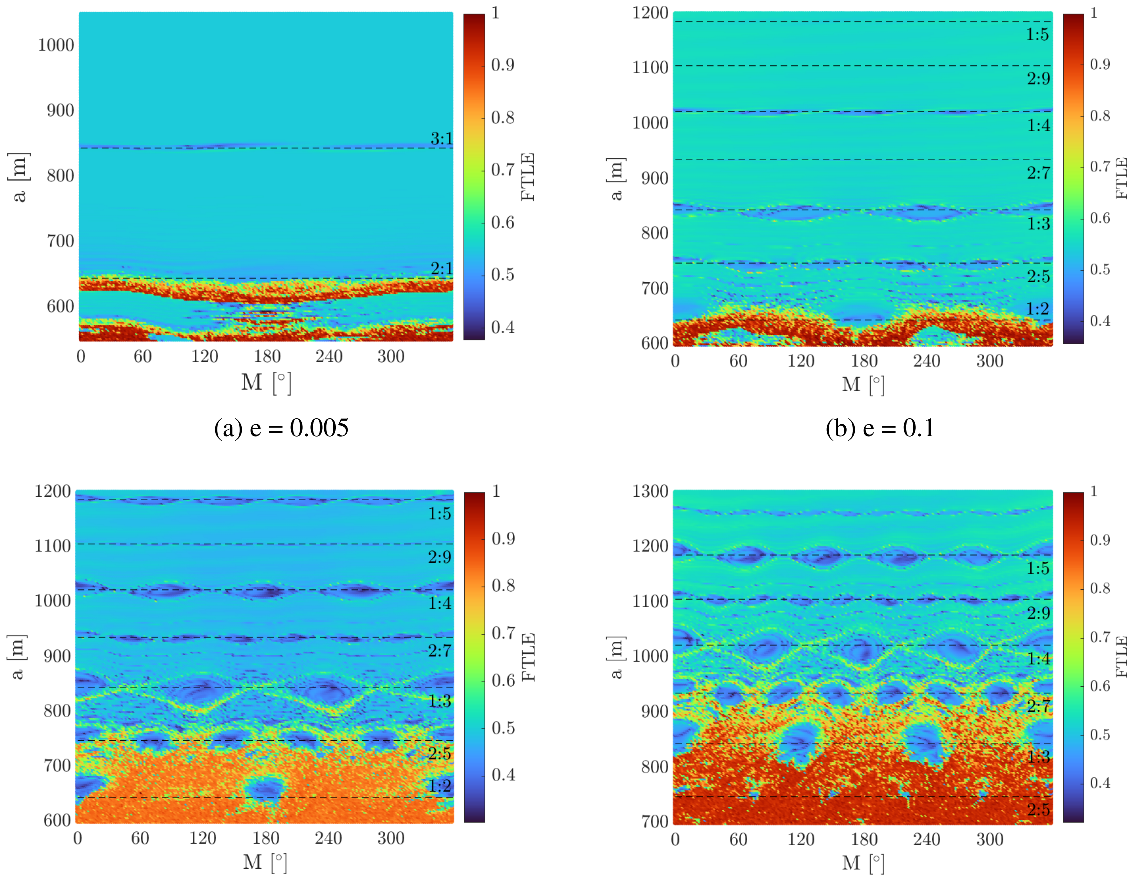

(a) e = 0.005

(b) e = 0.1

(c) e = 0.2

(d) e = 0.3

Figure 3: FTLE phase space plot in the (M, a) plane. The horizontal dashed lines represent the values of the $p_1 : p_2$ resonances at which the resonant structures are found. Plots for different values of eccentricities are reported.

Resonances in the $i = 0°$ case

The main resonances identified in the previous plots are here analyzed in terms of their amplitude of motion and stability for different values of eccentricity to provide an effective description of the dynamics in the neighborhood of a resonance. For each resonance, the corresponding Hamiltonian formulation is derived by determining the values of the integers n, m, p, q that define the p_1:p_2 resonance in terms of Kaula's resonant angle. From this, the location of the equilibrium points and the width of the resonance are computed. Stable and unstable equilibrium points are identified by solving the equations derived from the Hamiltonian:

$$\begin{cases} \dot{\sigma} = \dfrac{\partial H_{p_1:p_2}}{\partial L'} = 0 \\ \dot{L}' = -\dfrac{\partial H_{p_1:p_2}}{\partial \sigma} = 0 \end{cases} \tag{14}$$

Once the equilibrium points are known, the resonance width is computed as in.[10] Using the Hamiltonian value H_u corresponding to the unstable equilibrium point (σ_u, L_u) its level curve is traced on the phase space. This curve represents the separatrix, which divides libration and circulation regions. Along this separatrix, L reaches its maximum L_{max} and minimum L_{min} values at $\sigma = \sigma_s$, the stable equilibrium. The resonance width is then calculated as:

$$\Delta L = L_{\text{max}} - L_{\text{min}} \tag{15}$$

It should be noted that the position and number of equilibrium points, as well as the resonance amplitude, are highly sensitive to the number of harmonics retained in the Hamiltonian formulation of a given resonance. In particular, the influence of each individual term in the summation of Eq. 3 on the phase space can be readily examined, revealing how each contributes to features such as the location of equilibrium points and the resonance width. When all harmonics are considered simultaneously, the resulting phase space may no longer exhibit a well-defined pendulum-like structure; instead, it may take on a deformed shape, shaped by the combined effects of the most significant harmonics in the Hamiltonian. This can be observed in Fig. 4 where for the 1:4 resonance the Hamiltonian phase space plot appears deformed and with multiple equilibrium points, while for the 1:3 one it appears regular. The values of the equilibrium locations, and resonance widths are summarized in Tables 1, 2, 3, and 4 for different values of eccentricity.

Table 1: Equilibrium points locations and resonance widths for the main resonances for e = 0.005, $i = 0°$

p_1:p_2	σ_u [°]	a_u [m]	σ_s [°]	a_s [m]	ΔL [m]
1:3	170.6	846.3	846.3	349.2	1.5

Table 2: Equilibrium points locations and resonance widths for the main resonances for e = 0.1, $i = 0°$

p_1:p_2	σ_u [°]	a_u [m]	σ_s [°]	a_s [m]	ΔL [m]
2:5	55.6	749.9	750	193.3	24.0
1:3	157.3	846.2	352.0	846.4	33.6
2:7	202.1	937.4	25.2	937.4	4.1
1:4	171.7	1024	1024	350.3	12.3

Table 3: Equilibrium points locations and resonance widths for the main resonances for e = 0.2, $i = 0°$

p_1:p_2	σ_u [°]	a_u [m]	σ_s [°]	a_s [m]	ΔL [m]
2:5	746.0	88.2	747.0	87.1	103.0
	752.1	0.2	748.6	279.5	
1:3	105.5	847.1	149.1	847.1	68.1
	178.2	847.1	229.1	847.1	
	258.2	847.1	34	847.1	
	356.4	847.1	328	847.1	
2:7	191.1	937.5	51	937.5	23.1
1:4	154.0	1024	354.8	35.2	
2:9	199.3	1107.6	24.1	1107.6	7.4
1:5	168.9	1188	353.1	1188	19.3

Table 4: Equilibrium points locations and resonance widths for the main resonances for e = 0.3, $i = 0°$

p_1:p_2	σ_u [°]	a_u [m]	σ_s [°]	a_s [m]	ΔL [m]
1:3	95.5	857.2	44.1	836.4	180.35
	183.7	857.2	141.6	837.2	
	271.8	852	227.6	838	
	0	851	316.2	842	
2:7	357.5	938.6	81	938.6	84.1
	183.6	938.6	285	938.6	
1:4	105.2	1026.2	32.7	1023.1	72.2
	178.2	1025.2	149.1	1025.2	
	258.1	1024.1	229.1	1024.1	
	356.3	1023	327.3	1023	
2:9	191.6	1107.8	58.9	1107.7	29.3
1:5	138.5	1188.3	359.2	1188.3	43.2

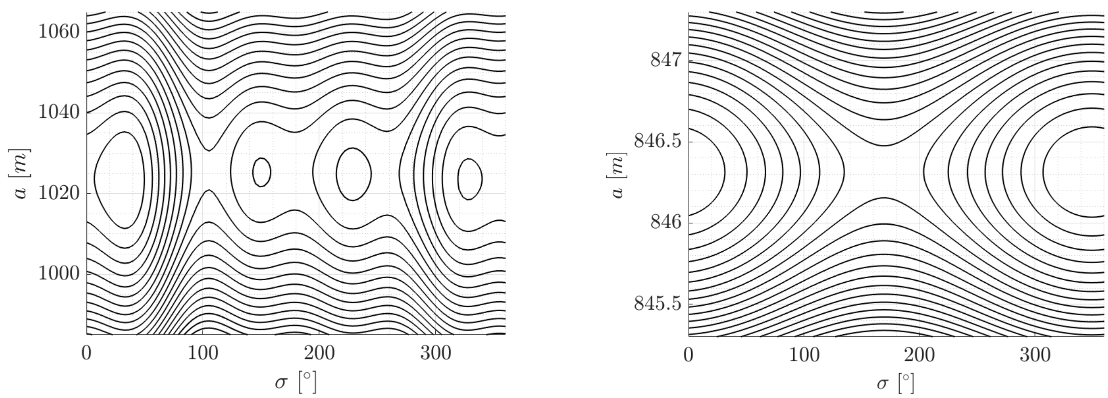

(a) e = 0.3, $i = 0°$, 1:4 resonance (b) e = 0.005, $i = 0°$, 1:3 resonance

Figure 4: Examples of Hamiltonian phase-space plot for two different resonances at different eccentricities. The black contour lines represent different energy values. Positions of stable and unstable equilibrium points can be easily identified.

Resonances in the $e = 0$ $(i \neq 0°)$ case

In the circular, inclined case, the same analysis is repeated for different values of inclination. Overall, the resulting plots are similar to those obtained in the low-eccentricity regime (see Fig. 3). The only clearly visible resonant feature in the phase space, aside from the chaotic region at low semi-major axis, is the 1:3 resonance island, which remains quite narrow.

Varying the inclination up to 20° does not significantly alter the global structure of the phase space. A close-up view of the 1:3 resonance in the FTLE phase space plot for $i = 20°$ is shown in Fig. 5.

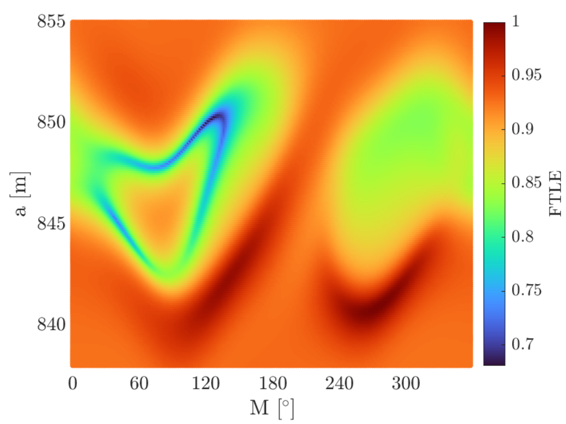

Figure 5: Zoom-in on the 1:3 resonance in the FTLE map for $e = 0$, $i = 20°$.

PARTICLE CAPTURE

To evaluate the likelihood of resonant capture in the resonant structures previously identified for the case of debris around a small body, Monte Carlo simulations are carried out. The dynamical model includes the full gravitational potential of Didymos, expanded up to degree and order 6, along with a perturbative term in the form of a Stokes-like drag to account for the effect of inter-particle interactions and their role in enabling particle capture:

$$\gamma = -\eta\dot{\theta}\left(-\lambda\mathbf{v}_t + \mathbf{v}_r\right) \tag{16}$$

where, $\mathbf{v}_r$ and $\mathbf{v}_t$ are the radial and tangential components of the particle velocity, respectively, η is a dimensionless friction coefficient, and λ is a tunable parameter that controls the balance between radial and tangential dissipation. This drag term acts as a simplified proxy for energy dissipation due to mutual collisions, following the approach proposed in.[11]

The introduction of the tangential term, absent in the original formulation of,[11] is motivated by the need to account for the non-radial nature of collisional interactions, as suggested by both physical intuition and N-body simulation results. When only radial dissipation is present (i.e., $\lambda = 0$), Gauss' planetary equations[12] predict a systematic damping of the eccentricity, which quickly drives the orbits toward circular configurations. This process effectively removes the dynamical structures associated with resonances in the phase space, thereby preventing the possibility of resonant capture. For this reason, including the tangential contribution proves essential to sustain moderate eccentricity values and preserve the necessary conditions for particles to become temporarily or permanently trapped within resonant regions.

The simulation setup is designed to mimic the dynamical evolution of an initially circular, equatorial disk of particles orbiting a rotating central body. In this context, collisions are expected to excite the particles' orbits, leading to an increase in both eccentricity and inclination, as supported by the findings of.[13] Specifically, comparisons with simulations performed using the REBOUND N-body integrator with hard-sphere collision models demonstrate that significant evolution in eccentricity, inclination, and semi-major axis occurs due to collisions. The tangential component in the drag force allows for tuning the dissipative response in a way that matches the secular trends observed in those simulations and in the outcomes discussed in.[13]

Tabs. 5 and 6 summarize the initial conditions adopted for two distinct Monte Carlo simulations, in which all orbital parameters are held fixed except for the true anomaly, which is sampled from a uniform distribution. The two simulations differ only in the value of the dissipation coefficient η.

Table 5: Parameters for particle capture analysis in the low dissipation case.

Parameter	**Value**
Semi-major axis range (a)	500 m
Eccentricity (e)	0
Inclination (i)	0°
Longitude of ascending node (Ω)	0°
Argument of periapsis (ω)	0°
True anomaly (ν)	0°–360°
MC samples	10000
Dissipation coefficient (η)	1e-3
Tangential coefficient λ	0.01
Captured particles	3.94 %

Table 6: Parameters for particle capture analysis in the high dissipation case.

Parameter	Value
Semi-major axis range (a)	500 m
Eccentricity (e)	0
Inclination (i)	0°
Longitude of ascending node (Ω)	0°
Argument of periapsis (ω)	0°
True anomaly (ν)	0°–360°
MC samples	10000
Dissipation coefficient (η)	0.01
Tangential coefficient λ	0.01
Captured particles	35.35 %

Both simulations reveal that, for a subset of particles, the semi-major axis tends to stabilize over time, as shown in Fig. 6, with some trajectories oscillating around values that correspond to resonant locations in phase space. A semi-major axis is considered stabilized if it exhibits bounded oscillations around a fixed value for more than 50 days. In the low-dissipation case (Tab. 5), the dominant resonances appear to be the 1:2 and 1:3, along with a resonance lying between the 2:5 and 1:2 commensurabilities. In the high-dissipation case (Tab. 6), also the 2:5 resonance becomes prominent, and the number of captured particles increases by almost an order of magnitude.

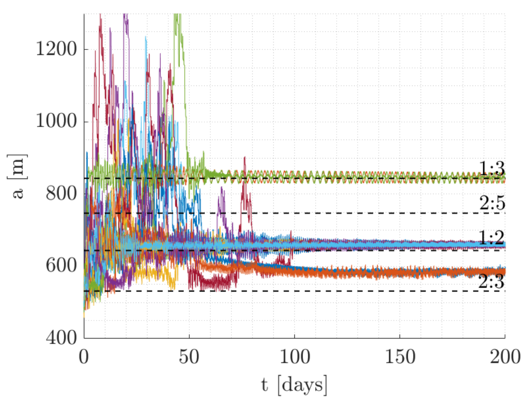

(a) Low dissipation simulation.

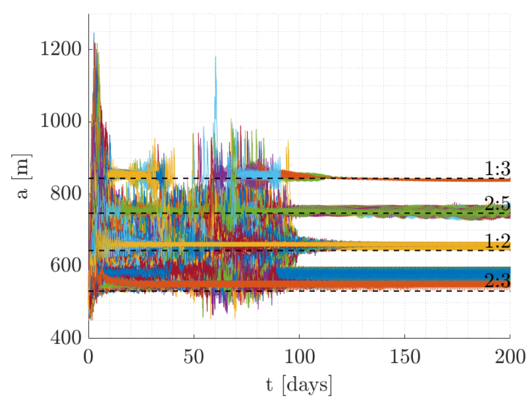

(b) High dissipation simulation.

Figure 6: Semi-major axis evolution of captured particles. Dashed horizontal lines represent the resonances locations.

For the subset of particles undergoing resonant capture, the evolution of eccentricity mirrors that of the semi-major axis. To illustrate this behavior, Fig.7 reports the time history of the semi-major axis, eccentricity, and inclination for two representative particles captured into the 1:2 and 1:3 resonances. Initially, chaotic fluctuations are observed, followed by a more regular behavior once capture occurs. In all cases, the final value of the eccentricity increases with respect to the initial circular orbit, consistently with the trends discussed previously. This observation further confirms the role of sustained moderate eccentricity, enabled by dissipative forcing, as a necessary condition for resonant trapping. It has been noted that in cases where the final eccentricity remains relatively low, the final inclination tends to be higher, as exemplified in Fig. 7b. As for inclination, most particles exhibit an overall increase over time. Unlike eccentricity, which in many cases shows a tendency to stabilize after resonance capture, the evolution of inclination appears to be more diverse. Some particles continue to increase their inclination after trapping, while others exhibit significant oscillations or even a decrease. This variability suggests that the mechanisms driving inclination and eccentricity excitation may operate differently and be influenced by distinct aspects of the dissipative dynamics. As such, the evolution of inclination following resonance capture does not show a universal trend and appears to be more sensitive to initial conditions and system parameters.

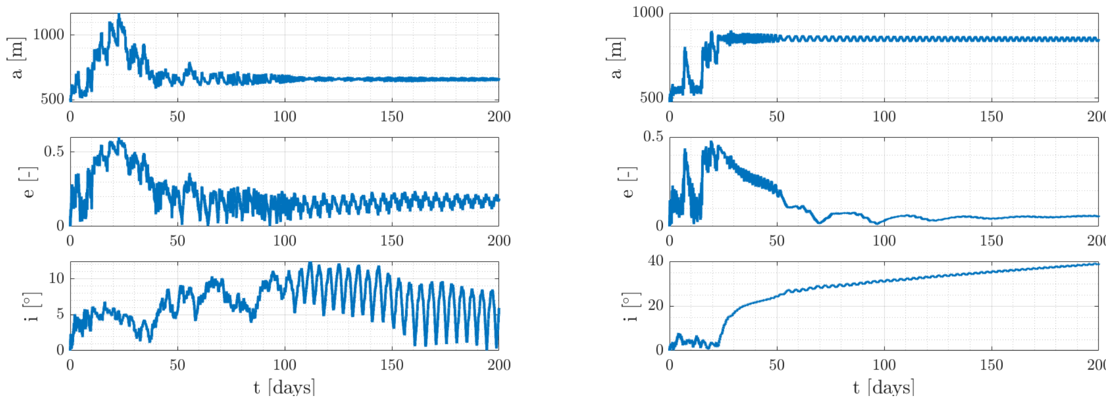

(a) 1:2 resonance.

(b) 1:3 resonance.

Figure 7: Orbital element variation for two particles trapped into a resonance.

Further insight into the resonant dynamics is provided by the phase-space representation in Fig.8, which shows the trajectory of a particle captured in the 1:3 resonance. Once captured, the motion becomes confined within the resonant region in the Hamiltonian phase space, and the particle exhibits librations around the stable equilibrium point associated with the resonance. This confinement confirms that the observed stabilization of semi-major axis corresponds to actual resonance locking rather than temporary dynamical features.

It is important to note that several particles exhibited transient captures, where temporary resonance locking was followed by escape. These cases have not been included in the analysis presented here.

CONCLUSION

This work aimed to characterize the dynamical environment around non-spherical small bodies by investigating how gravitational asymmetries shape the phase space structure. The analysis revealed the presence of resonant regions, islands of stability, and surrounding chaotic layers, whose location and extent depend sensitively on the orbital parameters. These dynamical features were mapped using a combination of Hamiltonian models, Poincaré sections, and numerical indicators, allowing a systematic identification of these structures. With regard to capture mechanisms, the results indicate that dissipation can promote resonance trapping, but only when sufficient orbital excitation, particularly in eccentricity, is maintained. Overall, the study emphasizes the interplay

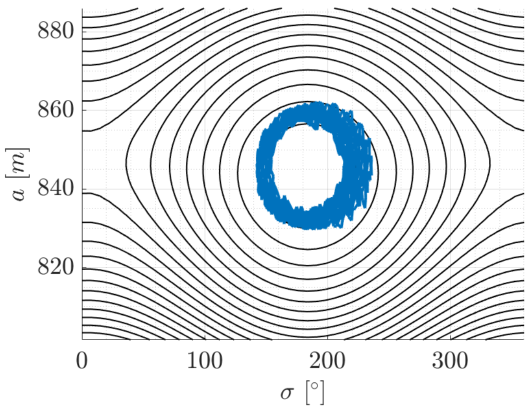

Figure 8: Phase-space trajectory of a particle captured in the 1:3 resonance. The blue points represent the evolution of the semi-major axis versus the $\sigma_{1:3}$ resonant angle. The trajectory remains confined within the resonant island and exhibits libration around the stable equilibrium point, confirming the occurrence of resonant trapping.

between resonance structures, chaotic diffusion, and dissipative effects in determining the transient or long-term retention of particles, with implications for the evolution of debris clouds, ring formation, and regolith dynamics around small bodies.

ACKNOWLEDGMENT

Funded by the European Union (ERC, TRACES, 101077758). Views and opinions expressed are however those of the author(s) only and do not necessarily reflect those of the European Union or the European Research Council. Neither the European Union nor the granting authority can be held responsible for them.

REFERENCES

[1] B. Sicardy, S. Renner, R. Leiva, F. Roques, M. El Moutamid, P. Santos-Sanz, and J. Desmars, "The dynamics of rings around Centaurs and Trans-Neptunian Objects," *The Trans-Neptunian Solar System*, pp. 249–269, Elsevier, 2020.

[2] W. Boumchita and J. Feng, "The capture probability of Dawn into ground-track resonances with Vesta," *Celestial Mechanics and Dynamical Astronomy*, Vol. 136, No. 1, 2024, p. 3.

[3] A. Celletti and C. Galeş, "On the dynamics of space debris: 1: 1 and 2: 1 resonances," *Journal of Nonlinear Science*, Vol. 24, 2014, pp. 1231–1262.

[4] G. Madeira, S. Giuliatti Winter, T. Ribeiro, and O. Winter, "Dynamics around non-spherical symmetric bodies–I. The case of a spherical body with mass anomaly," *Monthly Notices of the Royal Astronomical Society*, Vol. 510, No. 1, 2022, pp. 1450–1469.

[5] T. Ribeiro, O. Winter, G. Madeira, and S. Giuliatti Winter, "Dynamics around non-spherical symmetric bodies: II. The case of a prolate body," *Monthly Notices of the Royal Astronomical Society*, Vol. 525, No. 1, 2023, pp. 44–56.

[6] W. M. Kaula, *Theory of satellite geodesy: applications of satellites to geodesy*. Courier Corporation, 2013.

[7] C. D. Murray and S. F. Dermott, *Solar system dynamics*. Cambridge university press, 1999.

[8] G. Haller, "Lagrangian coherent structures," *Annual review of fluid mechanics*, Vol. 47, No. 1, 2015, pp. 137–162.

[9] J. Lages, D. L. Shepelyansky, and I. I. Shevchenko, "Chaotic zones around rotating small bodies," *The Astronomical Journal*, Vol. 153, No. 6, 2017, p. 272.

[10] J. Feng, R. Noomen, X. Hou, P. Visser, and J. Yuan, "1: 1 Ground-track resonance in a uniformly rotating 4th degree and order gravitational field," *Celestial mechanics and dynamical astronomy*, Vol. 127, No. 1, 2017, pp. 67–93.

[11] B. Sicardy, R. Leiva, S. Renner, F. Roques, M. El Moutamid, P. Santos-Sanz, and J. Desmars, "Ring dynamics around non-axisymmetric bodies with application to Chariklo and Haumea," *Nature Astronomy*, Vol. 3, No. 2, 2019, pp. 146–153.

[12] H. D. Curtis, *Orbital mechanics for engineering students*. Butterworth-Heinemann, 2019.

[13] H. F. Agrusa, Y. Zhang, D. C. Richardson, P. Pravec, M. Ćuk, P. Michel, R.-L. Ballouz, S. A. Jacobson, D. J. Scheeres, K. Walsh, *et al.*, "Direct N-body Simulations of Satellite Formation around Small Asteroids: Insights from DART's Encounter with the Didymos System," *The Planetary Science Journal*, Vol. 5, No. 2, 2024, p. 54.